APS physics

CHORUS

This is the accepted manuscript made available via CHORUS. The article has been published as:

Microscopic origin of pressure-induced isosymmetric transitions in fluoromanganate cryolites

Nenian Charles and James M. Rondinelli

Phys. Rev. B **90**, 094114 — Published 24 September 2014

DOI: 10.1103/PhysRevB.90.094114

Microscopic origin of pressure-induced isosymmetric transitions in fluoromanganate cryolites

Nenian Charles[1,*] and James M. Rondinelli[1,2,†]

[1] *Department of Materials Science & Engineering, Drexel University, Philadelphia, PA 19104, USA*
[2] *Department of Materials Science & Engineering, Northwestern University, Evanston, IL 60208, USA*

Using first-principles density functional theory calculations, we investigate the hydrostatic pressure-induced reorientation of the Mn–F Jahn-Teller bond axis in the fluoride cryolite Na_3MnF_6. We find a first-order isosymmetric phase transition (IPT) occurs between crystallographically equivalent monoclinic structures at approximately 2.15 GPa, consistent with earlier experimental studies. Mode-crystallography analyses of the pressure-dependent structures in the vicinity of the transition reveal a clear evolution of the Jahn-Teller bond distortions in cooperation with an asymmetrical stretching of the equatorial fluorine atoms in the MnF_6 octahedral units. We identify a significant (70%) change in the orbital occupancy of the e_g manifold of the $3d^4$ Mn(III) to be responsible for the transition, stabilizing one monoclinic $P2_1/n$ variant over the other. The orbital reconstruction as a driving force for the transition is confirmed by analogous calculations of isostructural $3d^0$ Na_3ScF_6, which shows no evidence of an IPT up to 6.82 GPa.

PACS numbers: 61.50.Ks, 74.62.Fj, 71.15.Mb

I. INTRODUCTION

Perovskite transition metal compounds with ABX_3 stoichiometry, where X is either oxygen or fluorine, have been extensively studied owing to their ability to support a rich set of physical phenomena ranging from multiferroisim to superconductivity[1–4]. Many of these properties are a direct consequence of structural phase transitions and symmetry reductions, which alter chemical bonding pathways and electronic properties through distortions and rotations of BX_6 octahedra through strong electron-lattice coupling. Indeed, the physical properties of perovskites can be tailored by changing the bonding environments by manipulating the BX_6 size, shape, and connectivity[5] using chemical pressure or epitaxial strain[6–9]. Thus, for electronic function engineering purposes it is useful to understand the tendency of a perovskite to distort, or undergo a structural transitions, which can be estimated using the Goldschmidt tolerance factor[10].

The tremendous success of perovskites has sparked interest in a closely related set of materials, the $A_2BB'X_6$ double perovskites with multiple cations that order among various planes in a periodic fashion (Fig. 1). The additional degree of freedom from compositional ordering not found in simple perovskites[11,12] can be used to obtain desirable ferroic responses[13,14], and explore correlated electron properties[15–17]. It is important to note that while there are a multitude of studies on perovskites and double perovskites, most of the materials physics literature is keenly focused on X=O transition metal oxides.[1] Fluoride compounds, however, also show an affinity for functional electronic behavior, including mutiferroicity[18–21], ionic conductivity[22]. Yet these ternary fluorides have received considerably less attention than their oxide counterparts although they are ferroelastic[23] and exhibit polymorphism.[24] As such, their properties are structure and symmetry dependent, albeit they tend to adopt the ideal undistorted structure more frequently.[25]

For the case of rock salt ordered double perovskites with two possible B cations (B and B′) with X = F (fluorine), these compounds are generally referred to by one of the two prototypes illustrated in Fig. 1. The first class being *cryolite*, after the compound Na_3AlF_6[26]. This family contains compounds with 12-coordinate A sites, whereby the same cation on the A site is chemically identical to one at the octahedrally coordinated B site (A = B), while the B′ cation remains unique. This results in the stoichiometry $A_3B'F_6$ for cryolite, and as a result the B cation interactions are 'interrupted' by the A cation occupying the B sublattice. The other prototype is *elpasolite*, which is named for the mineral K_2NaAlF_6.[27] It also refers to structures with 12-fold coordinated A cations, but unlike cryolite, the two octahedrally coordinated B sites are chemically distinct species (B and B′).[28,29] Thus the stoichiometry for elpasolite is $A_2BB'F_6$.

Here we focus on the cryolite Na_3MnF_6 (tolerance factor of 0.89), which possesses a strong first-order active Jahn-Teller d^4 Mn^{3+} cation and exhibits a distorted monoclinic $P2_1/n$ (space group 14) structure with both in-phase and out-of-phase MnF_6 octahedral rotations in its ground state (Fig. 2).[30] It is ferroelastic and experimentally undergoes an isostructural first-order monoclinic-to-monoclinic phase transition with hydrostatic pressure[31]. Such isostructural/isosymmetric phase transitions (IPT) without symmetry reductions[32] infrequently occur in inorganic condensed matter phases—displacive transitions are much more common[33]. Microscopic origins for such transitions include spin-state transitions,[34] electronic or magnetic polarization rotation,[35] or from bond reconfigurations due to mechanical epitaxial strain constraints.[36–40] For example, IPTs in Mn-based complex oxides have been reported to be induced by chemical pressure,[41] surface effects in nanoparticles,[42] and thermal cycling by melting an orbitally ordered state.[43] In such cases, the driving force is either a reduction in an electric polarization ($YMnO_3$)

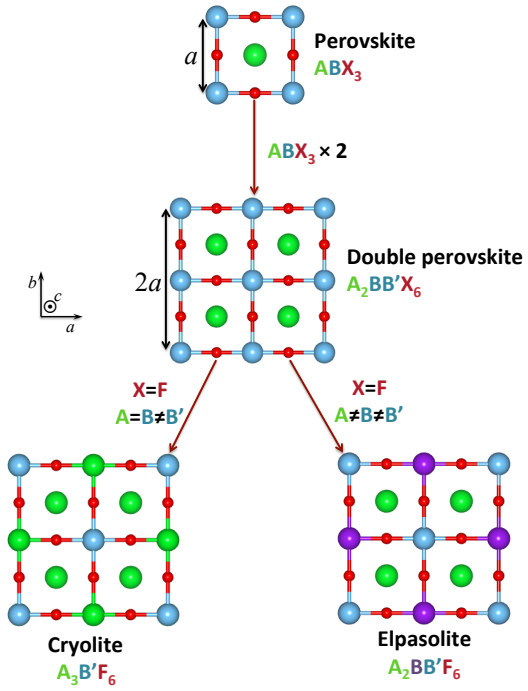

FIG. 1. Ideal structures of the double perovskite fluorides cryolite ($A_3B'F_6$, left) and elpasolite ($A_2BB'F_6$, right) as they relate to the cubic ABX_3 perovskite structure (top).

or due to the *removal* of the Jahn-Teller distortion altogether.

The IPT in Na_3MnF_6 is experimentally found to be reversible while showing characteristic first order hysteric behavior. Above and below the critical pressure value for the phase transition, the authors of Ref. 31 identified that the short and long Mn–F bond lengths, which are signatures of the Jahn-Teller distortion, persisted across the transition. Unlike the related oxides, the bond distortions remain and only the relative orientation of the distorted bond pairs with respect to the monoclinic axes switch. What are the atomic and electronic features responsible for the phase transition: is it due to spontaneous strain, the Mn electronic degrees of freedom, or strong electron–lattice interactions? We are unaware of a theory that captures the microscopic origin of this IPT in Na_3MnF_6 or related manganites where the Jahn-Teller distortion is not removed across the isosymmetric transition.

Herein, we use density functional theory calculations to identify the microscopic origin of the pressure-induced IPT in the fluoromanganate Na_3MnF_6. We find that the ground state monoclinic structure is stabilized through a combination of energy lowering MnF_6 octahedral rotations and Jahn-Teller (JT) bond elongations; the latter arise to remove the orbital degeneracy owing to electron occupation of the majority spin $e_g^{\uparrow}$-manifold presented by a cubic crystal field. These combined effects produce a crystal structure at ambient pressure that exhibits elongated Mn–F bonds along the long, crystallographic c axis depicted in Fig. 2(b), and is common for manganates with axial ratios $c/a > 1$.[44,45]

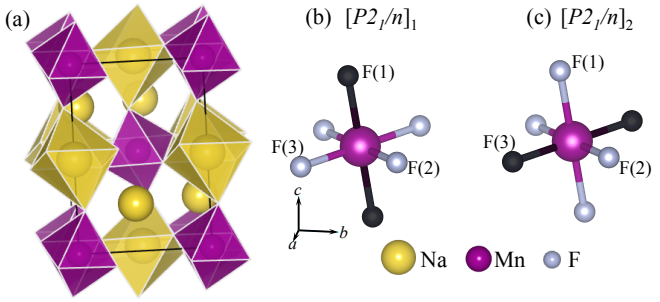

FIG. 2. Equilibrium zero kelvin structure of Na_3MnF_6, and the MnF_6 octahedra of the (b) low pressure $[P2_1/n]_1$ and (c) high pressure $[P2_1/n]_2$, phases. The long Mn–F bond axis, referred in the text as the Jahn-Teller (JT) bond axis, is highlighted in black and the ferrodistortive packing of these octahedra along the c-axis is the distinguishing structural feature across the monoclinic-to-monoclinic transition.

Upon application of hydrostatic pressure, we find a reorientation of the long JT Mn–F bond occurs for unit cell volumes of 240 ± 0.1 Å^3, corresponding to an experimental pressure between 2.10 GPa and 2.15 GPa in agreement with Ref. 31. At the electronic structure level, we find that the low-pressure fluoromanganate phases have fully occupied $d_{z^2-r^2}$ orbitals, whereas in the high-pressure phase, the occupancy reverses to be predominately of $d_{x^2-y^2}$ orbital character. Unlike previously reported IPTs in manganites, the Jahn-Teller mode is always present and the strong orbital-lattice coupling facilitates the electronic transition, which is marked by a giant (70%) change in the orbital polarization of the Mn e_g manifold through a renormalization of the mode stiffness of the Jahn-Teller distortion. Uncovering the microscopic origins of the transition sheds light on the effect of stress on the magnetic, electronic and structural degrees of freedom in Na_3MnF_6, but more broadly it reveals the Jahn-Teller distortion need not be removed across such transitions and hence well-defined orbitally ordered state may exists across such phase boundaries in related phases.

II. COMPUTATIONAL & SIMULATION DETAILS

We performed density functional theory calculations with the general gradient approximation (GGA) of Perdew-Burke-Ernzerhof revised for solids[46] (PBEsol) as implemented in the Vienna *Ab initio* Simulation Package (VASP)[47,48] with the projector augmented wave (PAW) method[49] to treat the core and valence electrons using the following valence configurations: $2p^6 3s^1$ for Na, $3p^6 4s^1 3d^6$ for Mn, and $2s^2 2p^5$ for F. We used a $7 \times 7 \times 7$ Monkhorst-Pack k-point mesh[50] with Gaussian smearing (0.1 eV width) for the Brillouin zone (BZ) integrations and a 600 eV plane wave cutoff. Spin-polarized structural relaxations were performed until the Hellmann-Feynman forces were less than 1 meV Å^{-1} for each atom position.

Magnetic Order. The long-range spin order for Na_3MnF_6 has not been previously reported. Therefore, prior to carrying out the pressure study, we explored the energetics for A-type antiferromagnetic order (in-plane ferromagnetic coupling between Mn sites, with out-of-plane antiferromagnetic coupling) and ferromagnetic order on the monoclinic $P2_1/n$ (ambient) structure with the JT Mn–F bond directed along the c axis. These two magnetic configurations are compatible with the 20 atom unit cell used in all calculations. From our total energy calculations of the fully relaxed phases, we find that the ferromagnetic configuration is essentially degenerate with the antiferromagnetic configuration: There is less than 0.1% difference in cell volume and an energy difference of 0.4 meV per formula unit (f.u.). These small differences between the magnetic variants also persist for calculations performed at elevated pressures. Owing to the strong ionic character of the fluoride and the fact that there appears to be very weak spin–lattice coupling, we use structures with ferromagnetic (FM) order throughout to perform the hydrostatic pressure simulations. As described below, the FM order yields excellent agreement with experimental structural data.

Application of Hydrostatic Pressure. We computationally mimic the experimental hydrostatic pressure study by imposing the lattice constants and monoclinic angles reported in Ref. 31 while allowing the internal coordinates to fully relax to obtain the total energies for both the low-pressure ($[P2_1/n]_1$) and high-pressure ($[P2_1/n]_2$) phases. Throughout we distinguish between the two phases by using the space group label with an additional index, 1 or 2, appended to the end to indicate if it is the low-pressure (phase 1) or high-pressure (phase 2) Na_3MnF_6 structure. The starting atomic configuration for the $[P2_1/n]_1$ phases employ the positions obtained from our fully relaxed zero pressure DFT-PBEsol simulations, whereas for the $[P2_1/n]_2$ structural relaxations, we initialize the atomic positions to those reported experimentally.[31]

III. RESULTS

A. Na_3MnF_6 Equilibrium Structure

Before performing the hydrostatic pressure study on Na_3MnF_6, we first determine the equilibrium structure at zero pressure with ferromagntic spin order. Consistent with experiments, we find a distorted monoclinic structure with in-phase MnF_6 octahedral rotations about the c axis and out-of-phase tilts. The combination of rotations and tilts gives the $a^-a^-c^+$ tilt pattern as described within Glazer notation[51]. Table I shows that the PBEsol functional provides an accurate description of the structural parameters of Na_3MnF_6 when compared to experiment. The error in the cell volume is ∼0.05%, under the constraint that the PBEsol structure has the same monoclinic angle as that reported in Ref. 30.

TABLE I. Comparison between the internal coordinates given in reduced units and lattice parameters a, b, and c (Å) for monoclinic Na_3MnF_6 ($P2_1/n$) obtained from DFT-PBEsol calculations and x-ray synchrotron experiments.[30] The monoclinic angle, $\beta = 88.96°$, is constrained to the experimental value. The unit cell volumes obtained from DFT and experiment are 251.09 and 250.97 Å^3, respectively. The Mn and Na(1) cations occupy the Wyckoff positions (WP) $2a(0,0,0)$ and $2b(0,0,1/2)$, respectively without free parameters, while all other atoms are free to displace.

Atom	WP		PBEsol	Experiment[30]
Na(2)	4e	x	0.510	0.509
		y	0.058	0.055
		z	0.750	0.750
F(1)	4e	x	0.122	0.115
		y	-0.063	-0.058
		z	0.761	0.767
F(2)	4e	x	0.722	0.719
		y	0.828	0.829
		z	-0.058	-0.053
F(3)	4e	x	0.162	0.163
		y	0.724	0.721
		z	0.068	0.067
a			5.472	5.471
b			5.684	5.683
c			8.075	8.073

To understand the complex atomic distortions in the monoclinic phase, we first recognize that a group–subgroup relationship exists between the ideal high-symmetry cubic structure without octahedral distortions or rotations, $Fm\bar{3}m$, and the $P2_1/n$ structure.[52] Mode crystallographic analysis[53,54] then enables us to determine the full set of unique symmetry-adapted mode displacements active in the $Fm\bar{3}m \rightarrow P2_1/n$ transition (see Fig. 3 for schematic illustrations), described as irreducible representation (irreps) of $Fm\bar{3}m$. We find that the cubic-to-monoclinic symmetry reduction requires a combination of at least two of these modes; based on the physical character (Fig. 3) and distortion mode amplitudes (Table SI of the Supplementary Material available in Ref. 25) of the modes present in the ground state structure, we deduce that the symmetry reduction is driven by out-of-phase octahedral rotations about the b axis and in-phase rotations about c-axis, *i.e.*, $\Gamma_4^+ \oplus X_3^+$.

B. Hydrostatic Pressure-induced Isosymmetric Transition

We investigate phase stability of the monoclinic Na_3MnF_6 by computing the total energy at various volumes for both the $[P2_1/n]_1$ and $[P2_1/n]_2$ structures.[55] Fig. 4 shows that the energy of both monoclinic phases increases with increasing pressure (decreasing cell volume).

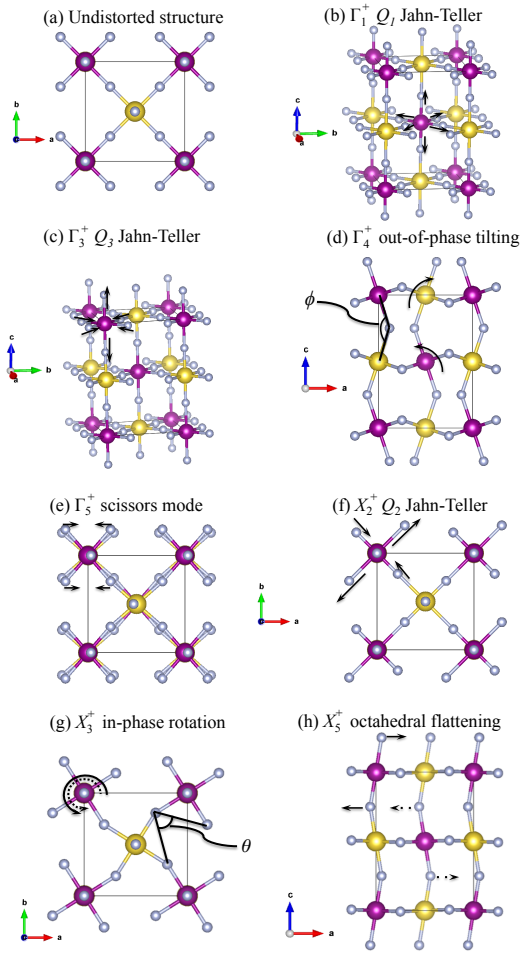

FIG. 3. Illustration of symmetry-adapted mode displacements which appear in monoclinic Na_3MnF_6 labeled according to irreps of the undistorted (a) $Fm\bar{3}m$ structure: (b) Γ_1^+: the Q_1 Jahn-Teller (JT) mode commonly referred to as the breathing distortion. (c) Γ_3^+: the Q_3 (two out–four in) JT vibrational mode. (d) Γ_4^+: the out-of-phase tilting of octahedra about the b axis. The tilt angle is measured as $(180° - \phi)/2$. (e) Γ_5^+: "scissor" mode which brings equatorial F anions in the MnF_6 octahedra closer together and reducing the intra-octahedral F–Mn–F bond angle from the ideal 90°. (f) X_2^+: the Q_2 (two in–two out) bond stretching mode in the ab plane. (g) X_3^+: in-phase rotations of the octahedra about the c axis. The rotation angle is measured as $(90° - \theta)/2$. (h) X_5^+: anti-parallel apical F displacements which lead to a flattening of the MnF_6 octahedra. Note that the Na(2) cations are excluded for clarity throughout, and broken lines indicate atomic displacements in the layer below.

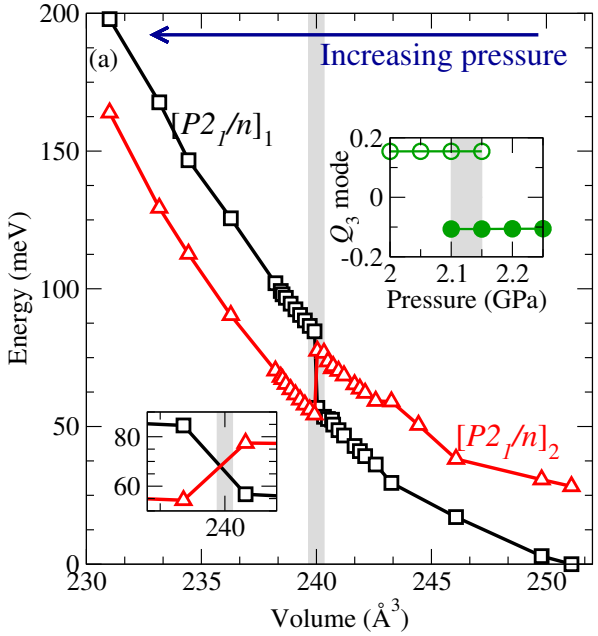

FIG. 4. Evolution of the total energy for the monoclinic $[P2_1/n]_1$ and $[P2_1/n]_2$ structures with cell volume given relative to the relaxed zero kelvin $[P2_1/n]_1$ ground state structure. The shaded region highlights the pressure domain of phase coexistence and the transition point about which the stability of the monoclinic phases reverses (see inset, left). The inset (right) shows the evolution of the Q_3 JT mode with pressure near the transition.

At low-pressure $[P2_1/n]_1$, exhibiting the Jahn-Teller bond axis oriented along the c axis, is more stable than $[P2_1/n]_2$ (JT bond axis in the ab plane) by ∼20 meV. This energetic stability remains until near the unit cell volume of 240 Å, where we find that both monoclinic structures are stable within our simulations. Upon further increase in pressure, $[P2_1/n]_2$ is stabilized relative to $[P2_1/n]_1$ by nearly the same energetic difference. From our mode crystallographic analyses, we find that the Q_3 irrep has the largest response at the transition, exhibiting both a discontinuity and sign change [Fig. 4 (inset)]. (We explore the energetics of this mode in more detail below.) We observe no change in space group symmetry or occupied Wyckoff positions for all volumes computed, consistent with available experimental results, which makes this transition isosymmetric.

We now explore changes in the internal atomic positions with pressure, focusing on the cooperative behavior of the Mn–F octahedra. We first examine the changes in the Mn–F bond lengths. Rather than using the symmetry-mode description, we parameterize the structural distortions to the MnF_6 octahedra in terms of first-order Jahn-Teller (JT) elongations Q_2 and Q_3[56]. This allows us to describe the JT modes by the position of the surrounding ligands in an octahedral field whose normal coordinates are associated with the vibrational mode that leads to a crystalline field removing the orbital degeneracy. The Q_2 mode is a tetragonal "two-in and two-out" bond distortion in the ab plane [$Q_2 > 0$, Fig. 3(c)], while Q_3 is a three-dimensional "two-out and four-in" bond distortion [$Q_3 > 0$, Fig. 3(f)].

In Na_3MnF_6, the Q_2 and Q_3 vibrational modes are ferrodistortively aligned. In the monoclinic systems studied here, the $Q_2 > 0$ mode elongates the Mn–F bonds that lie mainly along the b axis and shortens those along a, while $Q_3 > 0$ shortens the Mn–F bonds in the ab plane while elongating the bonds along c axis.

We obtain the fraction of the Q_2 and Q_3 JT modes

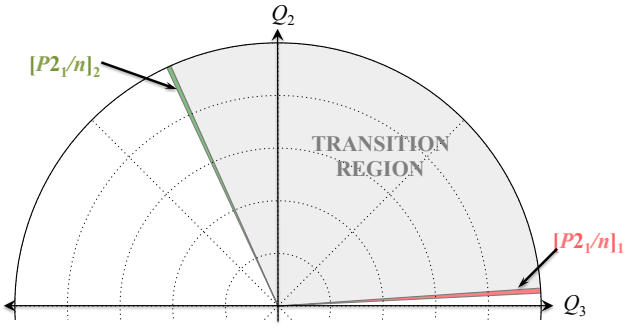

FIG. 5. Phase stability of $[P2_1/n]_1$ and $[P2_1/n]_2$ represented in the $Q_2 - Q_3$ plane of the Jahn-Teller lattice distortions. The red, green, and gray wedges illustrate the stability regions for $[P2_1/n]_1$, $[P2_1/n]_2$, and the transition region, revealing each structure is characterized by a dominant Q_2 or Q_3 mode.

present in the stable monoclinic low- and high-pressure variants as a function of hydrostatic pressure by computing the magnitude of the Jahn-Teller normal modes as follows:

$$Q_2 = \frac{2}{\sqrt{2}}[\mathrm{F}(3) - \mathrm{F}(2)],$$
$$Q_3 = \frac{2}{\sqrt{6}}[2\mathrm{F}(1) - F(2) - \mathrm{F}(3)]\,,$$

where, F(1), F(2), and F(3) are the Mn–F bond lengths directed along the c, a, and b axes, respectively. The JT phase is defined by $\Theta = \tan^{-1} Q_2/Q_3$. Within this formalism, $\Theta = 0°$ represents a JT distortion of octahedra stretched along the c axis. Angles of $\Theta = \pm 120°$ correspond to JT distortions along the b and a axis, respectively[44,45,57].

Fig. 5 shows the stability of the monoclinic Na_3MnF_6 structures in the Q_2-Q_3 plane. For $[P2_1/n]_1$, $\Theta = 2.99°$ at ambient pressure and evolves to a maximum of value of 4.06° at the critical pressure. Thus in the low pressure Na_3MnF_6 phase, the Q_3 JT mode dominates the Q_2 mode, leading to a tetragonal distortion of the MnF_6 octahedra that also elongates the c axis and contracts the crystal in the ab plane. Across the IPT there are no intermediate values of Θ (grayed region). In the high pressure phase $[P2_1/n]_2$, a drastic increase in the value of Θ occurs, *i.e.*, $\Theta = 114.1°$ and reaches a maximum of $\Theta = 115.0°$, which suggests a first order transition to a Q_2-type JT distortion and is consistent with the long bond becoming the Mn–F(3) bond as observed in the $[P2_1/n]_2$ phase.

C. Jahn-Teller Electronic Effects

We now investigate the electronic structure evolution across the IPT to understand the coupling between the electron and lattice degrees of freedom in Na_3MnF_6. Here, Mn(III) is found in a high-spin d^4 configuration with one electron in the e_g manifold, which appears as a strong

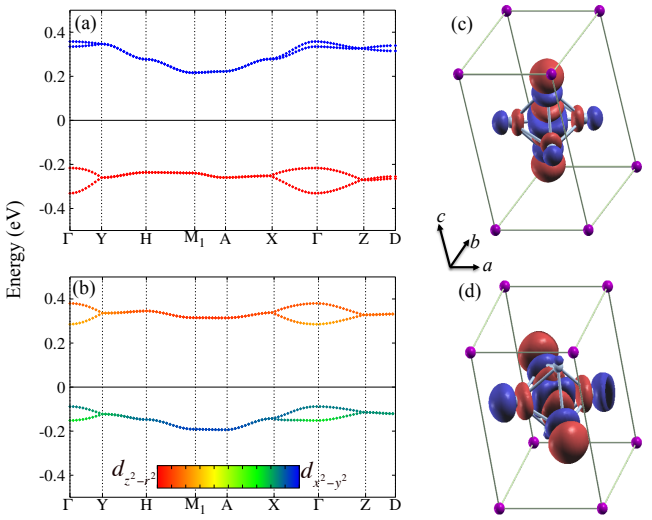

FIG. 6. Low energy electronic band structure about the Fermi level (horizontal line at 0 eV) with the projected e_g orbital character for Na_3MnF_6 at (a) $[P2_1/n]_1$ (0.0 GPA), and (b) $[P2_1/n]_2$ (2.5 GPa). The MLWF for the occupied molecular orbital for the (c) $[P2_1/n]_1$ and (d) $[P2_1/n]_2$.

Jahn-Teller distortion in the octahedra.[58–60] Thus, we anticipate that hydrostatic pressure directly affects the value of Θ in the Q_2-Q_3 subspace. Importantly, the value of Θ also provides a measure of the average character of the occupied molecular orbital state $|\Theta\rangle$ of the Jahn-Teller ion for a given static cooperative JT distortion as an arbitrary superposition of the e_g orbitals wave functions.[44,61] It can be approximated for a system at absolute zero as[57]

$$|\Theta\rangle = \cos(\Theta/2)\,|d_{z^2-r^2}\rangle + \sin(\Theta/2)\,\left|d_{x^2-y^2}\right\rangle\,.$$

We now use Maximally Localized Wannier Functions (MLWF)[62,63] to transform our periodic wave functions forming the valence band (VB) and conduction band (CB) edges into a local real-space representation of the e_g ($d_{x^2-y^2}$ and $d_{z^2-r^2}$) orbitals. The subspace is spanned by these atomic-like orbitals for the two Mn cations in the unit cell to evaluate the percent character of each orbital contributing to $|\Theta\rangle$.

Fig. 6(a) shows the electronic band structure near the Fermi level (E_F) for $[P2_1/n]_1$ at ambient pressure. The occupied bands are largely $3d_{z^2-r^2}$-like Mn states while the $3d_{x^2-y^2}$ orbital forms the conduction band throughout the Brillouin zone (BZ). It is significant to note that $\Theta = 2.99°$ for $[P2_1/n]_1$ at ambient pressure and this corresponds to $|\Theta\rangle$ being comprised of 99.9% $d_{z^2-r^2}$ orbital character in agreement with the MLWF projection Fig. 6(a). This result is characteristic of the orbital splitting anticipated with $Q_3 > 0$, where the apical bonds in the MnF_6 octahedra are elongated and the equatorial bonds contract[45]. The MLWFs reveal strong localization of the atomic like $3d_{z^2-r^2}$ orbital on the Mn cations below E_F [Fig. 6(c)]; the majority spin $e_g^{\uparrow}$ electron occupies the

TABLE II. Symmetry-adapted mode amplitudes (in Å) present in the equilibrium Na_3MnF_6 $[P2_1/n]_2$ phase at 2.50 GPa obtained from DFT-PBEsol calculations. The mode amplitudes are normalized with respect to the parent $Fm\bar{3}m$ structure.

Mode	Space group (number)	DFT-PBEsol
Γ_1^+	$Fm\bar{3}m$ (225)	0.119
Γ_3^+	$I4/mmm$ (139)	0.103
Γ_4^+	$C2/m$ (12)	1.465
Γ_5^+	$C2/m$ (12)	0.219
X_2^+	$P4_2/mnm$ (136)	0.083
X_3^+	$P4/mnc$ (128)	0.892
X_5^+	$Pnnm$ (58)	0.786

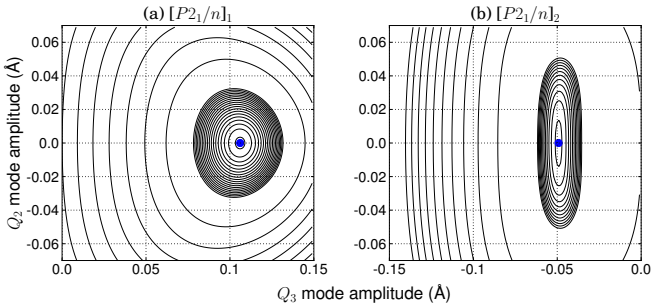

FIG. 7. Calculated two-dimensional energy surface contours for (a) $[P2_1/n]_1$ at ambient pressure and (b) $[P2_1/n]_2$ at 2.50 GPa with respect to the amplitude of the Q_2 and Q_3 JT modes derived from mode crystallography. The filled (blue) circles denote the position of minima in the potential energy surface.

orbital directed along the long JT-bond to reduce the Coulombic repulsion induced by the F $2p$ electron cloud.

Fig. 6(b) depicts the electronic structure for $[P2_1/n]_2$ at 2.50 GPa. From the projection onto the MLWFs, we observe in the high pressure phase that the VB and CB adopt mixed e_g-orbital character throughout the BZ. The occupied orbital, although dominated by atomic $d_{x^2-y^2}$ character, has an admixture of $d_{z^2-r^2}$ [Fig. 6(d)]. At 2.50 GPa, $\Theta = 114.2°$ in $[P2_1/n]_2$ and this angle predicts a wavefunction with 29.5% $d_{z^2-r^2}$ orbital character—a 70% change in the orbital polarization. The mixed e_g molecular orbital state is typical for manganates with a Q_2-like JT distortion, *i.e.*, the long-JT bond axis is oriented in the ab plane.[45,64,65]

We now examine the energetics associated with the changes in $|\Theta\rangle$ by computing the $Q_2 - Q_3$ energy surface (Fig. 7). We achieve this by incrementally increasing the Q_2 (X_2^+) and Q_3 (Γ_3^+) symmetry-adapted mode amplitudes in the $[P2_1/n]_1$ phase at ambient pressure[25] and $[P2_1/n]_2$ at 2.50 GPa (Table II) with respect to the undistorted reference structures.[66] In Fig. 7, mode amplitudes of $Q_2 > 0$ represent a JT distortion which elongates the Mn–F(3) bond and shortens the Mn–F(2) bonds in the ab plane, while $Q_2 < 0$ shortens Mn–F(3) and elongates Mn–F(2). Similarly, $Q_3 > 0$ mode amplitudes corresponds to a two-out–four-in JT distortion, which stretches the apical Mn–F(1) while shortening the Mn–F(2) and Mn–F(3) equatorial bonds. Conversely, $Q_3 < 0$ gives the four-out–two-in JT bonding environment that elongates bonds in the ab plane [Mn–F(2) and Mn–F(3)] and shortens the Mn–F(1) bond.

Considering only JT modes in the equilibrium volume of $[P2_1/n]_1$ at ambient pressure, we find a single energy minimum at $Q_3 \sim 0.11$ and $Q_2 = 0$ [Fig. 7(a)]. In this phase, a two-out–four-in Q_3 JT vibrational mode stabilizes Na_3MnF_6 at ambient pressure by approximately 38.6 meV/f.u. over the undistorted phase, which is consistent with the structural and electronic investigations already described. Despite having a small finite amplitude of Q_2 (X_2^+) present in the equilibrium structure,[25] Fig. 7(a) indicates that in the absence of other distortions any nonzero amplitude of Q_2 leads to an energetic penalty in $[P2_1/n]_1$. Thus, an asymmetric Mn–F bond stretching in the ab plane is an unfavorable distortion at ambient conditions without the presence of another distortion.

From Fig. 7(b), we observe that our two-dimensional energy surface predicts a single energy minimum for $[P2_1/n]_2$ at 2.50 GPa. Here, the minimum is located at $Q_3 \sim -0.048$ and $Q_2 = 0$. In the stable $[P2_1/n]_2$ phase it is noteworthy that the stability regime for the Q_3 vibrational mode is in a negative range. This indicates that unlike the $[P2_1/n]_1$ phase, at high pressures beyond the IPT a four-out–two-in Q_3 and not a two-out–four-in Mn–F distortion is required to stabilize the structure. According to the JT theory, a d^4 cation with $Q_3 < 0$ distortion splits the e_g degeneracy by occupying the $d_{x^2-y^2}$ orbital. Thus, the change in sign of the Q_3 mode is in accord with the $d_{x^2-y^2}$ state forming the valence band edge as observed in our calculations (Fig. 6). However, since $Q_2 = 0$ in the absence of any other distortion, at high pressure Na_3MnF_6 would exhibit four equivalent equatorial bonds, *i.e.*, Mn–F(2) = Mn–F(3), in the reduced subspace. The latter is in contrast to the fully relaxed atomic and electronic structure of the $[P2_1/n]_2$ phase. The MnF_6 octahedra exhibit multiple distortions with an approximately $Q_2 > 0$-like JT bonding environment. Indeed, the symmetry-adapted mode amplitudes for Na_3MnF_6 at 2.50 GPa (Table II) indicate that the Q_2 mode (X_2^+) is finite and larger in amplitude ($Q_2 = 0.083$) than at ambient pressure ($Q_2 = 0.056$).

We now seek to identify which other structural distortion (non-Jahn-Teller) acts to stabilize nonzero Q_2 mode amplitudes in the equilibrium structures. From the mode decomposition analysis at ambient and elevated pressure, we observe that the largest contribution to the equilibrium structures arise from the tilt (Γ_4^+) and rotation (X_3^+) of the MnF_6 units. To understand the nature of the tilt–Q_2 and rotation–Q_2 coupling, we incrementally increase the mode amplitude of Q_2 at finite amplitudes of the tilt and rotation (0%, 50%, 80%, 90% and 100% of their maximum) with respect to the undistorted reference structure.

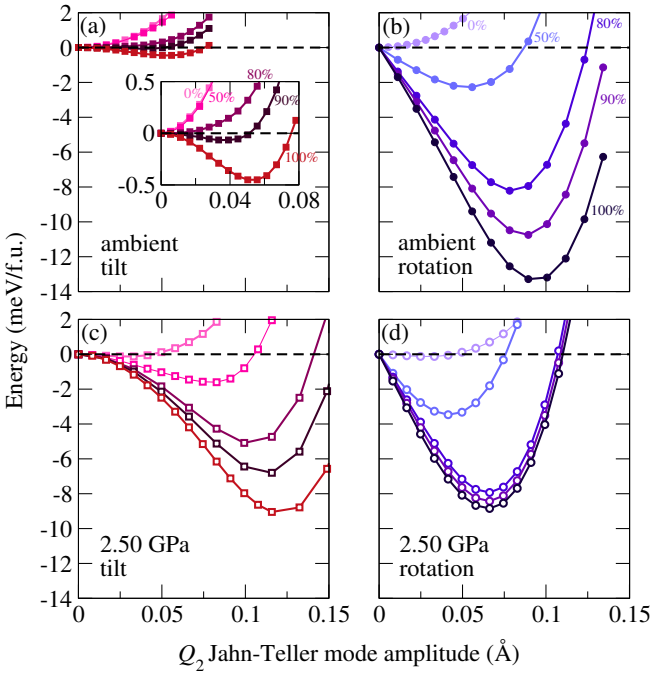

FIG. 8. Energy evolution from the coupling of the Q_2 Jahn-Teller distortion to the tilt and rotation at (a) and (b) ambient pressure (filled symbols) and at (c) and (d) 2.50 GPa (unfilled symbols), respectively. Normalized energy gain obtained by increasing the amplitude of the Q_2 mode at fixed percentages of the out-of-phase tilt [panels (a) and (c)] and in-phase rotations [panels (b) (d)] found in the ground equilibrium structures.

Fig. 8 shows that both the tilt and rotation modes couple to Q_2 and give a net energy gain in the total energy in both pressure regimes at finite amplitude. From Fig. 8(a) we observe that as the amplitude of tilt distortion increases in $[P2_1/n]_1$, the curvature of the Q_2 free energy evolves from a positive parabola with a single minimum at the $Q_2 = 0$ to a double-well potential with negative curvature about the origin and minima at finite Q_2 for tilt amplitudes $\geq 80\%$. This signifies a continuous softening of the Q_2 phonon mode induced by large amplitudes of the tilt mode (Γ_4^+ irrep), which effectively stabilizes the finite value of the asymmetric stretching observed in the ground state through a fourth-order biquadratic anharmonic interaction that renormalizes the mode stiffness of the quadratic Q_2^2 mode. The behavior of the MnF_6 rotation–Q_2 coupling in Fig. 8(b) shows that there is a large energetic gain associated with increasing amplitudes of the rotation mode. The single minima of the parabolic energy curves indicate, however, that while this coupling contributes to the total energy it does not soften the Q_2 mode frequency, but rather shifts the mode amplitude of Q_2 to a non-zero value through a linear-quadratic interaction.

In the high pressure phase (2.50 GPa) phase [Fig. 8(c) and (d)], we observe that the Q_2 irrep is unstable with a small energy gain < 1 meV at both 0% tilt and rotation amplitudes. Fig. 8(c) shows that increasing the amplitude of the tilt distortion in $[P2_1/n]_2$ leads to an enhanced energy stabilization, which ultimately promotes a larger Q_2 distortion in the high pressure phase. In contrast, increasing the contribution of the rotational mode hardens the Q_2 mode, the negative curvature at the origin is lost as shown in [Fig. 8(d)], and leads to a smaller amplitude of Q_2 through the coupled $Q_2^2 Q_{X_3^+}$ interaction.

IV. DISCUSSION

Our calculations and structural analysis indicate that the IPT is due to the spontaneous redistribution of the electronic charge density among the e_g orbitals of the strong JT Mn cation. There is a giant change in orbital occupation between the two isostructural variants owing to the persistent JT distortion across the transition. Specifically, we find that at low values of hydrostatic pressure the system is stabilized with the long bond along the c axis with a filled $d_{z^2-r^2}$ orbital which is characteristic of a $Q_3 > 0$ JT where $c/a > 1$[44,45]. Mode crystallographic analysis coupled with phenomenological Landau investigations of the JT Mn–F bond distortions reveals that the lattice strain induced by hydrostatic pressure renormalizes the mode stiffness of the JT vibrational modes across the transition. The leading coefficient of the harmonic Q_3^2 term of Hamiltonian changes sign under hydrostatic pressure.

Most significantly, we observe that across the transition the Q_3 JT irrep switches from a two-out-four-in ($Q_3 > 0$) in $[P2_1/n]_1$ to a four-out-two-in ($Q_3 < 0$) in the $[P2_1/n]_2$ phase. While the key structural signature defining $[P2_1/n]_2$ is a Q_2-like Mn–F bonding arrangement, we contend that the primary factor in the stabilization of the high pressure phase in Na_3MnF_6 is the change in sign of the Q_3 distortion mediated by the Q_2–MnF_6 tilt interaction. Table SI and Table II clearly show that the rotation amplitude is unchanged under pressure. Our electronic and phenomenological investigations indicate that at high pressure, it is more favorable for the charge to localize in the $d_{x^2-y^2}$-like orbital. Thus, the characteristic Q_2-like Mn–F_6 bonding distortion that differentiates the $[P2_1/n]_2$ and $[P2_1/n]_1$ phases is stabilized by second order effects. We show that a strong coupling exists between the tilt and Q_2 lattice degrees of freedom owing to an anharmonic interaction that stabilizes finite amplitudes of Q_2 in the equilibrium structures. The importance of this secondary effect is highlighted by comparing [Fig. 8(a) and (c)], as the energetic gain produced by the tilt–Q_2 coupling is increased approximately 20X in the $[P2_1/n]_2$ phase at equilibrium over the ambient case.

In addition, our electronic structure calculations show that hydrostatic pressure has an effect on the crystal field splitting in the stable phases of Na_3MnF_6. We observe that energy gap between the filled $d_{z^2-r^2}$ and the unoccupied $d_{x^2-y^2}$ is reduced from 0.43 eV at ambient pressure to 0.34 eV at the transition. Across the critical pressure for the transition, the band gap is 0.37 eV at 2.20 GPa.

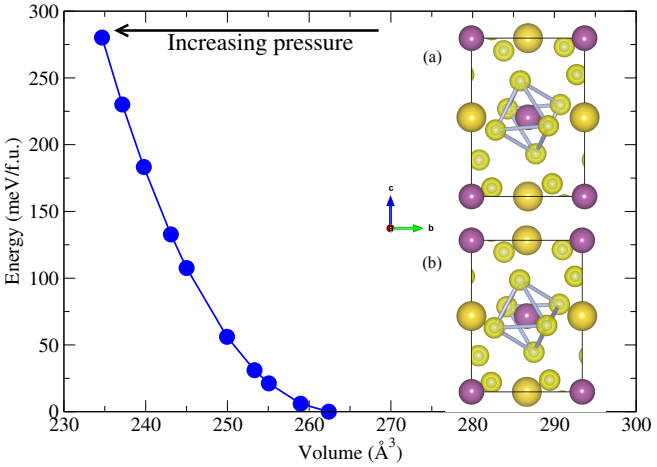

FIG. 9. Evolution of the total energy of Na_3ScF_6 with cell volume relative to the DFT relaxed ground state structure. The inset depicts the partial charge density obtained over the energy window ranging from -2 eV to E_F at (a) ambient pressure (0.0 GPa) and (b) 6.82 GPa. Unlike Na_3MnF_6, neither a structural transition nor charge redistribution is observed.

The continued application of hydrostatic pressure in the high pressure phase further decreases the band gap at approximately 0.02 eV/GPa which allows us to predict a insulator-to-metal transition around ∼20 GPa.

Based on this understanding, we performed a similar set of calculations for the d^0 compound Na_3ScF_6, which also crystallizes with $P2_1/n$ symmetry and for which experimental structural data under hydrostatic pressure exists.[67] We find there is no discontinuity in either the total energies (Fig. 9) or in the evolution of the Sc–F bond lengths up to a pressure of 6.82 GPa, which indicates that no isosymmetric transitions occur up to a pressure that is approximately 4.7 GPa higher than required for the fluoromanganate. Indeed, Fig. 9 shows the partial charge density for Na_3ScF_6 obtained by integrating over a finite region from -2 eV to E_F is highly uniform at both ambient Fig. 9(a) and high pressure Fig. 9(b). The absence of both a JT instability and an anisotropic bonding environment is consistent with the experimental findings and the proposed electronic origin for the IPT in Na_3MnF_6, highlighting the importance of the JT-active Mn(III).

V. CONCLUSION

We used first principles density functional calculations to study the electronic and atomic origins of the first-order pressure induced phase transition in Na_3MnF_6. We identified that the isosymmetric transition originates from two key features present in the fluoromangante: (i) a Jahn-Teller active Mn(III) ion with an e_g orbital degeneracy, and (ii) the strong coupling of the cooperative Mn–F bond distortions with hydrostatic pressure. We observe that while simple structural arguments may identify the $[P2_1/n]_1$ phase of Na_3MnF_6 as being dominated by a Q_3-type JT distortion and the $[P2_1/n]_2$ phase as Q_2-type, the combined effect of both distortions with collective MnF_6 tilts are essential to describing the stability of the structure at ambient and hydrostatic pressures.

In the $[P2_1/n]_1$ structures the $Q_3 > 0$ JT distortion splits the e_g manifold into atomic-like occupied $d_{z^2-r^2}$ and an unoccupied $d_{x^2-y^2}$ orbitals owing to an elongated JT Mn–F bond aligned along the crystallographic c-axis. After the transition to the high pressure phase $[P2_1/n]_2$, the JT-bond axis reorients into the ab plane with the structure largely characterized by a Q_2-type bonding arrangement. The transition above 2.15 GPa is arguably driven by a spontaneous renormalization of the Q_3 vibrational mode, *i.e.* $Q_3 < 0$. The equilibrium structure of the $[P2_1/n]_2$ phase is stabilized by secondary lattice effects which couple the tilt and Q_2 JT phonon modes to give the Mn–F(3) > Mn–F(1) > Mn–F(2) which is the signature of the high pressure phase of Na_3MnF_6.

This mechanism for the IPT drives a giant orbital reconstruction within the occupied $3d$ manifold of Mn^{3+}, whereby the JT distortion is always present in the structure. While it is understood that fluctuations in the orbital occupancy of the d orbitals can alter physical properties and drive structural transitions,[68] this study presents an interesting case were the orbital degrees of freedom are highly sensitive to the mechanical boundary conditions owing to the cryolite structure. Finding materials where it is possible to induce large changes in orbital polarization is an active area of research, because even small changes in orbital occupations particularly in thin films at surfaces and interfaces[69–72] can produce drastic variations in magnetic and transport properties. Given the extreme nature of the orbital reconstruction we observe with hydrostatic pressure, we anticipate our study will motivate new synthetic efforts focused on exploring Na_3MnF_6 and related magnetic cryolites in thin film form. Electronic structure calculations focused on evaluating the feasibility of epitaxial strain to induced the IPT are in progress.

ACKNOWLEDGMENTS

N.C. thanks Danilo Puggioni for useful discussions. N.C. and J.M.R. acknowledge the donors of The American Chemical Society Petroleum Research Fund for support (Grant No. 52138-DNI10). DFT calculation were performed on the high-performance computing facilities available at the Center for Nanoscale Materials (CARBON Cluster) at Argonne National Laboratory, supported by the U.S. DOE, Office of Basic Energy Sciences (BES), DE-AC02-06CH11357, and at the Extreme Science and Engineering Discovery Environment (XSEDE), which is supported by National Science Foundation Grant No. OCI-1053575.

* neniancharles@drexel.edu
† jrondinelli@northwestern.edu

[1] R. A. F. Pinlac, C. L. Stern, and K. R. Poeppelmeier, Crystals **1**, 3 (2011).
[2] A. T. Mulder, N. A. Benedek, J. M. Rondinelli, and C. J. Fennie, Advanced Functional Materials **23**, 4810 (2013).
[3] L. Qiao, K. H. L. Zhang, M. E. Bowden, T. Varga, V. Shutthanandan, R. Colby, Y. Du, B. Kabius, P. V. Sushko, M. D. Biegalski, and S. A. Chambers, Advanced Functional Materials **23**, 2953 (2013).
[4] L. Martin and R. Ramesh, Acta Materialia **60**, 2449 (2012).
[5] J. M. Rondinelli, S. J. May, and J. W. Freeland, MRS Bulletin **37**, 261 (2012).
[6] M. Imada, A. Fujimori, and Y. Tokura, Reviews of Modern Physics **70**, 1039 (1998).
[7] J. B. Goodenough, Chemistry of Materials **26**, 820 (2014).
[8] D. G. Schlom, L.-Q. Chen, X. Pan, A. Schmehl, and M. A. Zurbuchen, Journal of the American Chemical Society **91**, 2429 (2008).
[9] L. W. Martin, S. P. Crane, Y.-H. Chu, M. B. Holcomb, M. Gajek, M. Huijben, C.-H. Yang, N. Balke, and R. Ramesh, Journal of Physics: Condensed Matter **20**, 434220 (2008).
[10] V. M. Goldschmidt, Naturwissenschaften **14**, 477 (1926).
[11] M. T. Anderson, K. B. Greenwood, G. A. Taylor, and K. R. Poeppelmeier, Progress in Solid State Chemistry **22**, 197 (1993).
[12] G. King and P. M. Woodward, J. Mater. Chem. **20**, 5785 (2010).
[13] T. Saha-Dasgupta, Journal of Physics: Condensed Matter **26**, 193201 (2014).
[14] J. Young and J. M. Rondinelli, Chemistry of Materials **25**, 4545 (2013).
[15] O. Erten, O. N. Meetei, A. Mukherjee, M. Randeria, N. Trivedi, and P. Woodward, Phys. Rev. Lett. **107**, 257201 (2011).
[16] D. D. Sarma, P. Mahadevan, T. Saha-Dasgupta, S. Ray, and A. Kumar, Phys. Rev. Lett. **85**, 2549 (2000).
[17] O. N. Meetei, O. Erten, M. Randeria, N. Trivedi, and P. Woodward, Phys. Rev. Lett. **110**, 087203 (2013).
[18] J. Ravez, J. Phys. III France **7**, 1129 (1997).
[19] C. Ederer and N. A. Spaldin, Phys. Rev. B **74**, 020401 (2006).
[20] J. F. Scott and R. Blinc, Journal of Physics: Condensed Matter **23**, 113202 (2011).
[21] A. C. Garcia-Castro, N. A. Spaldin, A. H. Romero, and E. Bousquet, Phys. Rev. B **89**, 104107 (2014).
[22] J. Rau, K. Aliouane, M. Hamadne, A. Guehria, M. E. Omari, J. Grannec, and J. Ravez, Solid State Ionics **127**, 301 (2000).
[23] A. Tressaud, J. Portier, S. Shearer-Turrell, J.-L. Dupin, and P. Hagenmuller, Journal of Inorganic and Nuclear Chemistry **32**, 2179 (1970).
[24] G. King, A. M. Abakumov, P. M. Woodward, A. Llobet, A. A. Tsirlin, D. Batuk, and E. V. Antipov, Inorganic Chemistry **50**, 7792 (2011).
[25] See Supplemental Material at [URL will be inserted by publisher] for discussion of tolerance factor in double perovskite fluorides and additional mode amplitude data of the equilibrium phase.
[26] F. C. Hawthorne and R. B. Ferguson, The Canadian Mineralogist **13**, 377 (1975).
[27] L. R. Moras, Journal of Inorganic and Nuclear Chemistry **36**, 3876 (1974).
[28] I. Flerov, M. Gorev, K. Aleksandrov, A. Tressaud, J. Grannec, and M. Couzi, Materials Science and Engineering: R: Reports **24**, 81 (1998).
[29] W. Massa and D. Babel, Chemical Reviews **88**, 275 (1988).
[30] U. Englich, W. Massa, and A. Tressaud, Acta Crystallographica Section C **48**, 6 (1992).
[31] S. Carlson, Y. Xu, U. Hlenius, and R. Norrestam, Inorganic Chemistry **37**, 1486 (1998).
[32] J. F. Scott, Advanced Materials **22**, 2106 (2010).
[33] M. T. Dove, *Introduction to Lattice Dynamics* (Cambridge University Press, 1993) cambridge Books Online.
[34] A. G. Christy, Acta Crystallographica Section B **51**, 753 (1995).
[35] A. S. Gibbs, K. S. Knight, and P. Lightfoot, Phys. Rev. B **83**, 094111 (2011).
[36] Z. Chen, Z. Luo, C. Huang, Y. Qi, P. Yang, L. You, C. Hu, T. Wu, J. Wang, C. Gao, T. Sritharan, and L. Chen, Advanced Functional Materials **21**, 133 (2011).
[37] H. M. Christen, J. H. Nam, H. S. Kim, A. J. Hatt, and N. A. Spaldin, Phys. Rev. B **83**, 144107 (2011).
[38] J. M. Rondinelli and S. Coh, Physical Review Letters **106**, 235502 (2011).
[39] G. Gou and J. M. Rondinelli, Advanced Materials Interfaces (2014), 10.1002/admi.201400042.
[40] A. J. Hatt, N. A. Spaldin, and C. Ederer, Phys. Rev. B **81**, 054109 (2010).
[41] T.-Y. Tan, Q. Zhou, B. J. Kennedy, Q. Gu, and J. A. Kimpton, Solid State Sciences **14**, 506 (2012).
[42] S. Tripathi and V. Petkov, Applied Physics Letters **102**, 061909 (2013).
[43] Journal of Solid State Chemistry **182**, 2858 (2009).
[44] K. I. Kugel and D. I. Khomski, Soviet Physics Uspekhi **25**, 231 (1982).
[45] J. B. Goodenough, A. Wold, R. J. Arnott, and N. Menyuk, Phys. Rev. **124**, 373 (1961).
[46] J. P. Perdew, A. Ruzsinszky, G. I. Csonka, O. A. Vydrov, G. E. Scuseria, L. A. Constantin, X. Zhou, and K. Burke, Phys. Rev. Lett. **100**, 136406 (2008).
[47] G. Kresse and J. Furthmüller, Phys. Rev. B **54**, 11169 (1996).
[48] G. Kresse and D. Joubert, Phys. Rev. B **59**, 1758 (1999).
[49] P. E. Blöchl, Phys. Rev. B **50**, 17953 (1994).
[50] H. J. Monkhorst and J. D. Pack, Physical Review B **13**, 5188 (1976).
[51] A. M. Glazer, Acta Crystallographica Section B **28**, 3384 (1972).
[52] The occupied Wyckoff sites for Na_3MnF_6 in the $Fm\bar{3}m$ space group are 4*a* for Mn, 4*b* for Na(1), 8*c* for Na(2), and 24*e* for F.
[53] B. J. Campbell, H. T. Stokes, D. E. Tanner, and D. M. Hatch, Journal of Applied Crystallography **39**, 607 (2006).
[54] J. M. Perez-Mato, D. Orobengoa, and M. I. Aroyo, Acta Crystallographica Section A **66**, 558 (2010).
[55] Fine sampling near the reported[31] transition pressure is achieved by extrapolating best fit lines of the evolution of lattice parameters from the energetically more stable $[P2_1/n]_2$.
[56] J. H. Van Vleck, The Journal of Chemical Physics **7**, 72

(1939).
[57] J. Kanamori, Journal of Applied Physics **31**, S14 (1960).
[58] M. A. Carpenter and C. J. Howard, Acta Crystallographica Section B **65**, 134 (2009).
[59] J. B. Goodenough, Reports on Progress in Physics **67**, 1915 (2004).
[60] J. B. Goodenough, Annual Review of Materials Science **28**, 1 (1998).
[61] A. Stroppa, P. Barone, P. Jain, J. M. Perez-Mato, and S. Picozzi, Advanced Materials **25**, 2284 (2013).
[62] N. Marzari and D. Vanderbilt, Phys. Rev. B **56**, 12847 (1997).
[63] A. A. Mostofi, J. R. Yates, Y.-S. Lee, I. Souza, D. Vanderbilt, and N. Marzari, Computer Physics Communications **178**, 685 (2008).
[64] J. E. Medvedeva, M. A. Korotin, V. I. Anisimov, and A. J. Freeman, Phys. Rev. B **65**, 172413 (2002).
[65] Y. Murakami, J. P. Hill, D. Gibbs, M. Blume, I. Koyama, M. Tanaka, H. Kawata, T. Arima, Y. Tokura, K. Hirota, and Y. Endoh, Phys. Rev. Lett. **81**, 582 (1998).
[66] The undistorted structures are constructed to have cell volumes and monoclinic angles that correspond to the pressure being studied with all mode amplitudes equal to zero relative to the DFT-PBEsol relaxed monoclinic structures. The energy maps are obtained from 225 self-consistent total energy calculations and then fitting these points to a polynomial expansion in orders of Q_2 and Q_3.
[67] S. Carlson, Y. Xu, and R. Norrestam, Journal of Solid State Chemistry **135**, 116 (1998).
[68] Y. Tokura and N. Nagaosa, Science **288**, 462 (2000).
[69] T. Chatterji, F. Fauth, B. Ouladdiaf, P. Mandal, and B. Ghosh, Physical Review B **68**, 052406 (2003).
[70] A. Tebano, C. Aruta, S. Sanna, P. G. Medaglia, G. Balestrino, A. A. Sidorenko, R. De Renzi, G. Ghiringhelli, L. Braicovich, V. Bisogni, and N. B. Brookes, Physical Review Letters **100**, 137401 (2008).
[71] M. J. Han, C. A. Marianetti, and A. J. Millis, Phys. Rev. B **82**, 134408 (2010).
[72] E. Benckiser, M. W. Haverkort, S. Brck, E. Goering, S. Macke, A. Fra, X. Yang, O. K. Andersen, G. Cristiani, H.-U. Habermeier, A. V. Boris, I. Zegkinoglou, P. Wochner, H.-J. Kim, V. Hinkov, and B. Keimer, Nature Materials **10**, 189 (2011).